Stable Cesium Formamidinium Lead Halide Perovskites

Groeneveld, Bart G. H. M.; Adjokatse, Sampson; Nazarenko, Olga; Fang, Hong-Hua; Blake, Graeme R.; Portale, Giuseppe; Duim, Herman; ten Brink, Gert H.; Kovalenko, Maksym; Loi, Maria Antonietta

Published in:
Energy Technology

DOI:
10.1002/ente.201901041

Publication date:
2019

Energy Technology
Generation, Conversion, Storage, Distribution
www.entechnol.de

Stable Cesium Formamidinium Lead Halide Perovskites: A Comparison of Photophysics and Phase Purity in Thin Films and Single Crystals

*Bart G. H. M. Groeneveld, Sampson Adjokatse, Olga Nazarenko, Hong-Hua Fang, Graeme R. Blake, Giuseppe Portale, Herman Duim, Gert H. ten Brink, Maksym V. Kovalenko, and Maria Antonietta Loi**

The stability of the active layer is an underinvestigated aspect of metal halide perovskite solar cells. Furthermore, the few articles on the subject are typically focused on thin films, which are complicated by the presence of defects and grain boundaries. Herein, a different approach is taken: a perovskite composition that is known to be stable in single crystal form is used, and its (photo-)physical properties are studied in the form of spin-coated thin films. The perovskites are lead-based with cesium and formamidinium as the A-site cations and iodide and bromide as the halide anions, with the formula $Cs_{0.1}FA_{0.9}PbI_{3-x}Br_x$. These compounds show high potential in terms of stability in single crystal form and closely resemble the compounds that have successfully been used in highly efficient perovskite–silicon tandem solar cells. It is found that a small difference in bromine content ($x = 0.45$ vs 0.6) has a significant impact in terms of the phase purity and charge carrier lifetimes, and conclude that the thin films of $Cs_{0.1}FA_{0.9}PbI_{2.55}Br_{0.45}$ have good potential for the use in optoelectronic devices.

1. Introduction

The main strength of hybrid metal halide perovskite solar cells is their high power conversion efficiency, which can reach values over 25%.[1] However, an underdeveloped aspect of these devices is their stability, for which further investigation and improvement are needed. One of the most important aspects considered for improvement is the structural stability of the perovskite layer, which is influenced by the stoichiometry of the material and, therefore, also affects the environmental stability of the device.[2–5] A perovskite with low structural stability can be affected by degradation, for example, in the form of phase segregation.[6] An approach to improve the structural stability is to use elaborate compositions involving multiple cations or halide ions based on the Goldschmidt tolerance factor, which will be addressed later.[5,7–9] The caveat with this method is that, generally, perovskite solar cells are based on thin films. This brings more factors into the equation: the morphology of the layer and the presence of defects. The solution processes used to make perovskite thin films introduce defects into the layer, for example, in the form of grain boundaries, which have been correlated with the material's instability.[10] The choice of solvent, the use of anti-solvent, and the processing method can all influence the morphology, which in turn gives rise to different degrees of stability.[11] Therefore, to investigate the intrinsic stability of new perovskite compositions, it is possible to circumvent the variability of the morphology of thin films by using single crystals. Crystals typically have fewer defects that act as charge traps,[12,13] and are characterized by long-term stability.[2]

Here, we propose to select a metal halide perovskite that was previously synthesized in single crystal form to ensure that it is

B. G. H. M. Groeneveld, Dr. S. Adjokatse, Dr. H.-H. Fang, Dr. G. R. Blake, Dr. G. Portale, H. Duim, G. H. ten Brink, Prof. M. A. Loi
Zernike Institute for Advanced Materials
University of Groningen
Nijenborgh 4, Groningen 9747 AG, The Netherlands
E-mail: m.a.loi@rug.nl

The ORCID identification number(s) for the author(s) of this article can be found under https://doi.org/10.1002/ente.201901041.

DOI: 10.1002/ente.201901041

Dr. O. Nazarenko, Prof. M. V. Kovalenko
Department of Chemistry and Applied Biosciences
Laboratory of Inorganic Chemistry
ETH Zürich
Vladimir-Prelog-Weg 1, Zürich CH-8093, Switzerland

Dr. O. Nazarenko, Prof. M. V. Kovalenko
Laboratory for Thin Films and Photovoltaics
Empa – Swiss Federal Laboratories for Materials Science and Technology
Überlandstrasse 129, Dübendorf CH-8600, Switzerland

structurally stable and investigate how the material performs in spin-coated thin films.

A tool that can be used to predict a perovskite's stability is the Goldschmidt tolerance factor, which gives criteria for the radii of the ions that can fit in the structure.[14] For lead-based perovskites, the incorporation of cesium and formamidinium (FA) makes it possible to improve the Goldschmidt tolerance factor compared with a mixed halide perovskite based on the methylammonium (MA) cation, such as $MAPbI_{3-x}Br_x$. For example, the compositions $Cs_{0.15}FA_{0.85}PbI_3$, $Cs_{0.17}FA_{0.83}PbI_{1.8}Br_{1.2}$, and $Cs_{0.05}FA_{0.16}MA_{0.79}PbI_{2.49}Br_{0.51}$ have a better tolerance factor and, therefore, a higher stability.[5,7,9] $Cs_{0.17}FA_{0.83}PbI_{2.49}Br_{0.51}$ was used in a perovskite–silicon tandem solar cell with a power conversion efficiency of 23.6% and high environmental stability.[15]

Here, we investigate similar compounds, with composition $Cs_{0.1}FA_{0.9}PbI_{3-x}Br_x$ (where x is 0.45 or 0.6), of which the $x = 0.6$ variety was previously synthesized in single crystal form and demonstrated to be stable.[16] We report the first investigation on the $x = 0.45$ compound, which we anticipated to be similar to the higher bromine content perovskite in terms of structural stability. Because of the lower bromine ratio, we expected to have a broader absorption range due to a slightly narrower bandgap, which is favorable for multijunction photovoltaic applications. We find that these compounds are stable both as single crystals and thin films, which allows for a comparison of the photophysical and structural properties in each form. We also observe that there is a difference in phase purity of the spin-coated thin films. The higher bromine content perovskite has traces of the δ-phase of both $CsPbI_3$ and $FAPbI_3$—both non-perovskite phases—as determined by grazing-incidence wide-angle X-ray scattering (GIWAXS), whereas the material with the lower bromine content only has traces of the δ-phase of $FAPbI_3$. Time-resolved photoluminescence experiments indicate that the film containing both non-perovskite phases displays lower charge carrier lifetimes. Interestingly, more commonly applied techniques such as confocal laser scanning microscopy (CLSM) and energy-dispersive X-ray spectroscopy (EDX) cannot detect the impurities in our films. Based on all our data, we conclude that the lower bromine content material is the best choice for optoelectronic applications.

2. Results

$Cs_{0.1}FA_{0.9}PbI_{2.4}Br_{0.6}$ was selected for its structural stability, which is due to its favorable Goldschmidt tolerance factor ($t = 0.84$). $Cs_{0.1}FA_{0.9}PbI_{2.55}Br_{0.45}$ has a similar tolerance factor; therefore, we expected it also to be stable. The lower bromine content should lead to an absorption onset at longer wavelengths, which is beneficial for the use in multijunction photovoltaic devices. We verified this by measuring the optical properties of both compounds. **Figure 1**a shows the absorbance of both $Cs_{0.1}FA_{0.9}PbI_{2.55}Br_{0.45}$ and $Cs_{0.1}FA_{0.9}PbI_{2.4}Br_{0.6}$ in spin-coated thin films. The decreased bromide content of $Cs_{0.1}FA_{0.9}PbI_{2.55}Br_{0.45}$ leads to a redshift of about 20 nm. This is in agreement with previous literature, where higher bromide content leads to a wider bandgap material.[16] The photoluminescence (PL) spectra also show a redshift for the sample with the lower bromide content. Here, the shift between the two compositions is smaller (15 nm) compared with that for the absorbance spectra.

During the previously reported synthesis of $Cs_{0.1}FA_{0.9}PbI_{3-x}Br_x$ perovskites, impurities such as the non-perovskite δ-phases of $FAPbI_3$ and $CsPbI_3$ were found.[16] To verify that the compositions of our films are phase pure, X-ray diffraction (XRD) measurements were performed. Powder XRD measurements were unable to determine the crystal structures of the films: first, the peak intensities cannot be quantitatively analyzed due to the small sample volume probed in this geometry, and, second, the peaks are significantly broader than the instrumental resolution (Figure S1, Supporting Information), preventing the resolution of any peak splitting due to tetragonal distortion and making it difficult to detect any compositional inhomogeneity. Nonetheless, a weak unindexed peak at $2\theta = 11.7°$ in both patterns (Figure S2, Supporting Information), which corresponds to the (100) peak of the non-perovskite δ-$FAPbI_3$ phase (concentration around 1 wt%), is revealed.[5] However, no traces of δ-$CsPbI_3$ could be detected with powder XRD.

CLSM was used to verify that the films are free of δ-$CsPbI_3$. Because the non-perovskite phase of $CsPbI_3$ has broad photoluminescence ranging from 450 to 600 nm,[17] it will be discernable from the emission of the cesium–FA compounds. CLSM was performed to check the uniformity of the emission in terms of energy and intensity over the surface of the thin films

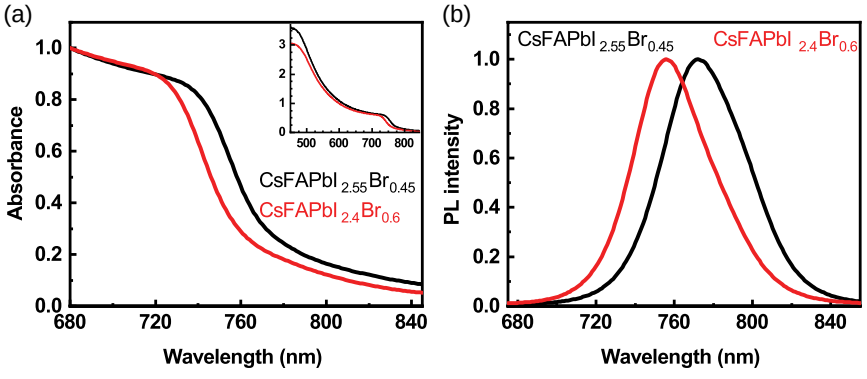

Figure 1. a) Normalized absorbance spectra of spin-coated thin film perovskites with compositions $Cs_{0.1}FA_{0.9}PbI_{2.55}Br_{0.45}$ (black lines) and $Cs_{0.1}FA_{0.9}PbI_{2.4}Br_{0.6}$ (red lines). The inset shows the absorbance over a longer range. b) Normalized photoluminescence spectra of the thin films with the same compositions as in part (a).

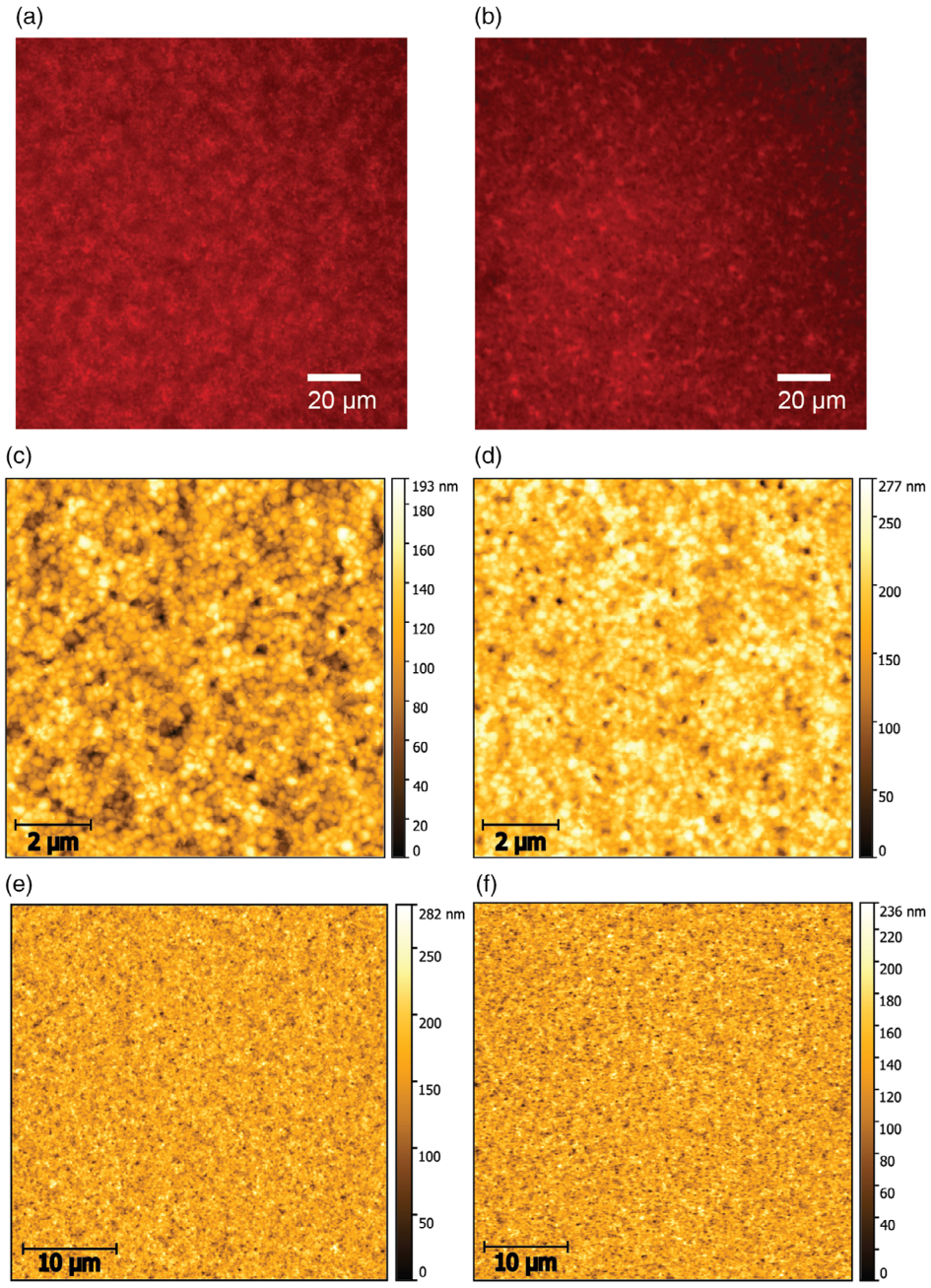

Figure 2. CLSM false-color images of thin films of a) $Cs_{0.1}FA_{0.9}PbI_{2.55}Br_{0.45}$ and b) $Cs_{0.1}FA_{0.9}PbI_{2.4}Br_{0.6}$. The photoluminescence signal in red is emitting within a 780 nm long-pass filter. Atomic force microscopy images of the morphology of thin films of $Cs_{0.1}FA_{0.9}PbI_{2.55}Br_{0.45}$ are shown in parts c) and e), and $Cs_{0.1}FA_{0.9}PbI_{2.4}Br_{0.6}$ in parts d) and f). The root mean square roughnesses calculated from these figures are 24, 26, 29, and 23 nm, respectively.

(**Figure 2**a,b). Because of the band pass filters used in the confocal setup, it is not possible to locate different compositions with only slight variations in the stoichiometry. However, the filter with a band pass of 590 ± 40 nm would be able to detect δ-$CsPbI_3$. From the photoluminescence maps, there are no traces of emission from δ-$CsPbI_3$: we only see the emission of the films in the 780 nm long-pass range. In addition, we looked for variations in emission intensity, which might indicate the presence of different phases that act as recombination sites. Both films have good uniformity in the photoluminescence signal, and the only variations arise from morphological features. The morphology was characterized using atomic force microscopy; images of the films are shown in Figure 2c–f. The films seem smooth with crystal grain sizes on the order of hundreds of nanometers: this is due to the high number of nucleation sites induced by the anti-solvent method during spin-coating.

The structure of the thin films was further studied by GIWAXS (see **Figure 3**a–d for 2D images). The GIWAXS patterns suggest that both thin films have an almost isotropic structure with only a weak orientation of the crystallites. Comparing

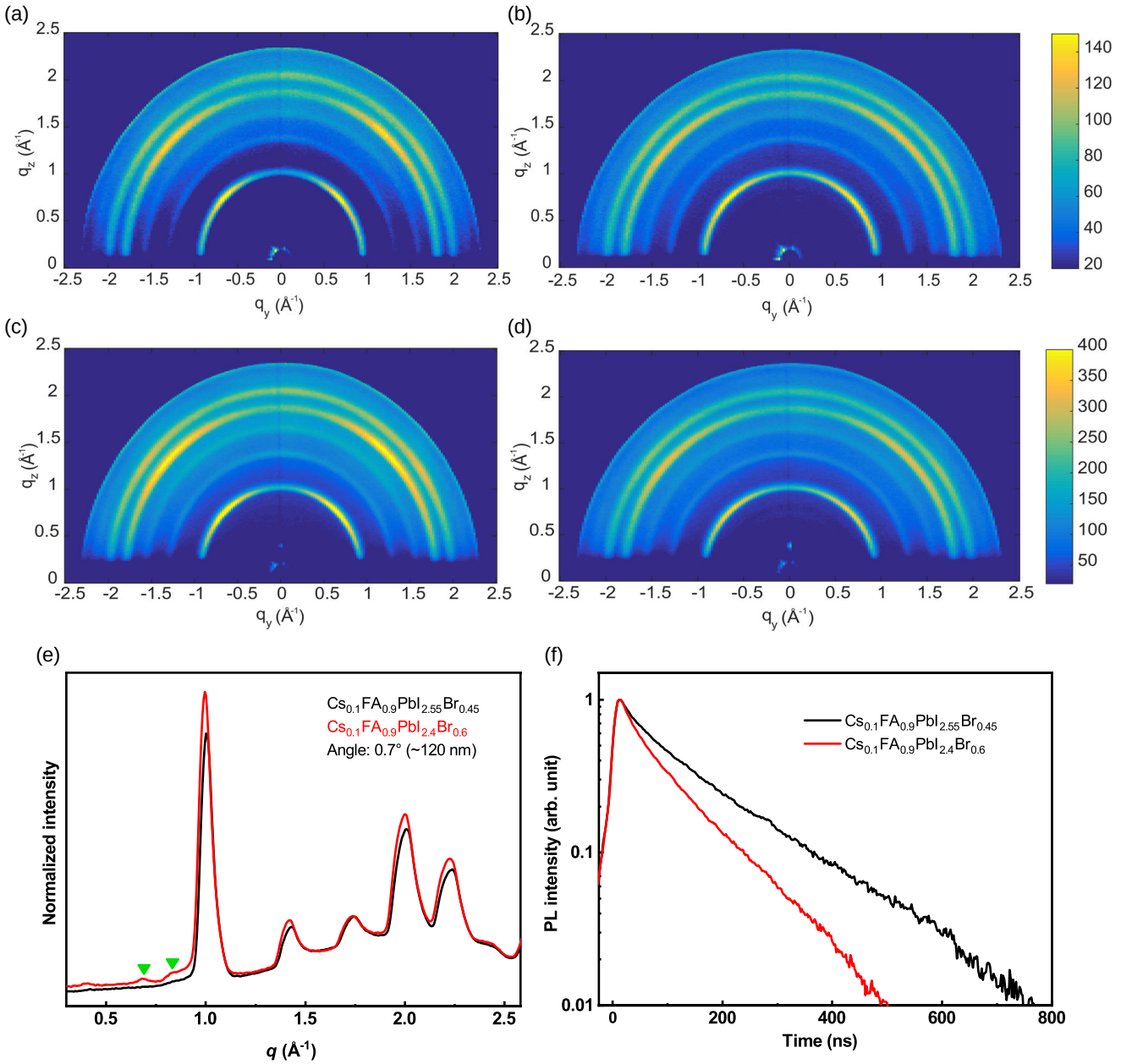

Figure 3. GIWAXS patterns of a) $Cs_{0.1}FA_{0.9}PbI_{2.55}Br_{0.45}$ measured at $\alpha_i = 0.4°$; b) $Cs_{0.1}FA_{0.9}PbI_{2.4}Br_{0.6}$ measured at $\alpha_i = 0.4°$; c) $Cs_{0.1}FA_{0.9}PbI_{2.55}Br_{0.45}$ measured at $\alpha_i = 2.1°$; and d) $Cs_{0.1}FA_{0.9}PbI_{2.4}Br_{0.6}$ measured at $\alpha_i = 2.1°$. e) GIWAXS integrated intensity plotted versus q (normalized at $q = 1.4$ Å^{-1}) for the thin films of $Cs_{0.1}FA_{0.9}PbI_{2.55}Br_{0.45}$ (black) and $Cs_{0.1}FA_{0.9}PbI_{2.4}Br_{0.6}$ (red). The incident angle was 0.7°, corresponding to a penetration depth of approximately 120 nm. The green triangles indicate the phases found only in $Cs_{0.1}FA_{0.9}PbI_{2.4}Br_{0.6}$. f) Time-resolved photoluminescence decay of both spin-coated films. The normalized data are plotted on a semilogarithmic scale. The lifetimes extracted from biexponential decay fits are $\tau_1 = 36.3$ ns and $\tau_2 = 178$ ns for $Cs_{0.1}FA_{0.9}PbI_{2.55}Br_{0.45}$ and $\tau_1 = 24.6$ ns and $\tau_2 = 116$ ns for $Cs_{0.1}FA_{0.9}PbI_{2.4}Br_{0.6}$.

the integrated intensity versus q plots in **Figure 4**e of $Cs_{0.1}FA_{0.9}PbI_{2.55}Br_{0.45}$ and $Cs_{0.1}FA_{0.9}PbI_{2.4}Br_{0.6}$, we can see that there are two additional peaks at low q values for the latter material: at $q = 0.69$ Å^{-1} and $q = 0.82$ Å^{-1}. These q values translate to 2θ angles of 9.7° and 11.5°, respectively. These peaks in the film with higher bromine content are attributed to two nonperovskite phases: the orthorhombic δ-phase of $CsPbI_3$ and the δ-phase of $FAPbI_3$.[5,18] These phases are present throughout the entire thickness of the $Cs_{0.1}FA_{0.9}PbI_{2.4}Br_{0.6}$ film, as shown by the presence of these peaks independently of the incident angle used to acquire the GIWAXS profiles (Figure S3, Supporting Information). Upon close inspection, we can also find the $q = 0.82$ Å^{-1} peak in the film of $Cs_{0.1}FA_{0.9}PbI_{2.55}Br_{0.45}$, confirming the results obtained with XRD that both films contain the δ-phase of $FAPbI_3$. However, no trace of the non-perovskite $CsPbI_3$ was found. Thus, $Cs_{0.1}FA_{0.9}PbI_{2.4}Br_{0.6}$ seems to be less

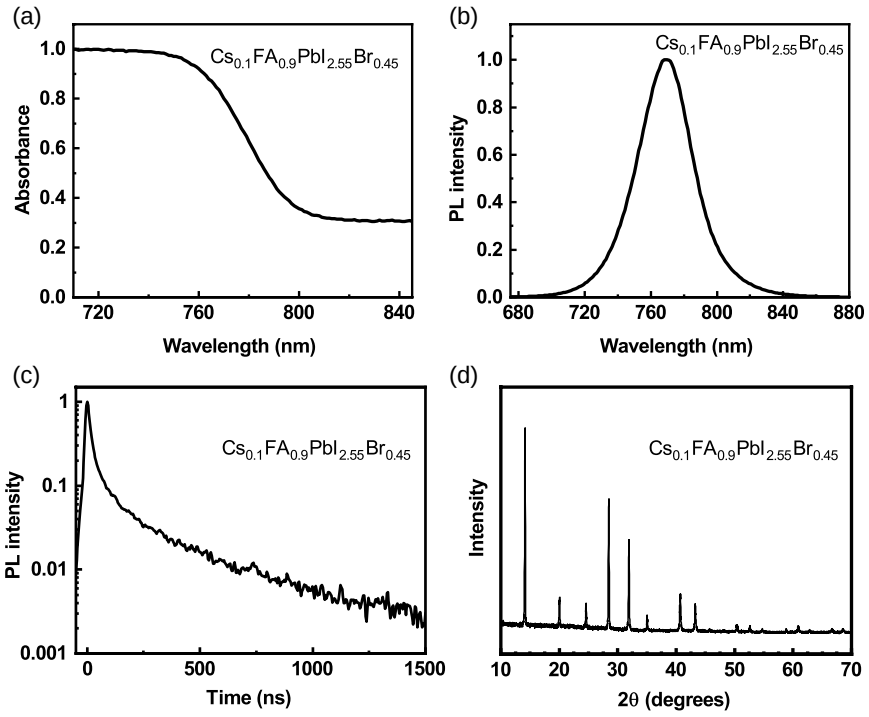

Figure 4. Characterization of the optical and structural properties of the $Cs_{0.1}FA_{0.9}PbI_{2.55}Br_{0.45}$ single crystal. a) Normalized absorbance onset. b) The steady-state and c) time-resolved photoluminescence measurements (normalized data). The steady-state emission is centered around 770 nm, with a FWHM of 39 nm. The PL decay in part (c) can be adequately described by a three-exponential decay, in which a strong initial decay ($\tau = 16$ ns) is followed by a much slower decay with time constants of $\tau = 30$ and $\tau = 267$ ns. d) The powder XRD pattern of the single crystal.

stable than $Cs_{0.1}FA_{0.9}PbI_{2.55}Br_{0.45}$ because it forms two different phases which do not contribute to the photocurrent in solar cells. The effect of these two unwanted phases on the charge carrier lifetimes was investigated with time-resolved photoluminescence experiments (Figure 3f). We find that the charge carrier lifetimes of $Cs_{0.1}FA_{0.9}PbI_{2.4}Br_{0.6}$ are much lower than those of $Cs_{0.1}FA_{0.9}PbI_{2.55}Br_{0.45}$, and we propose that the δ-phase of $CsPbI_3$ plays a decisive role here. Combining the longer charge carrier lifetimes, the higher crystalline quality, and the lower bandgap of $Cs_{0.1}FA_{0.9}PbI_{2.55}Br_{0.45}$, we can conclude that this is the most promising material for the use in optoelectronic devices.

EDX was used in an attempt to locate the two non-perovskite phases (δ-$FAPbI_3$ and δ-$CsPbI_3$) in the two films. This technique can be used to observe the spatial distribution of elements and has been used in previous studies on metal halide perovskites to study phase segregation. Examples are element maps of halogen atoms and of various inorganic atoms that are used in hybrid perovskite research.[19,20] The EDX spectra of the spin-coated layers of $Cs_{0.1}FA_{0.9}PbI_{2.55}Br_{0.45}$ and $Cs_{0.1}FA_{0.9}PbI_{2.4}Br_{0.6}$ are shown in Figure S4, Supporting Information. The resulting element maps are shown in Figure S5, Supporting Information. From the lack of order in the distribution of iodine, cesium, bromine, and lead, we conclude that there is no sign of phase segregation at this resolution, which gives an upper limit to the domain size of the impurities of 50 nm. From the full width at half maximum (FWHM) of the fitted peaks in the GIWAXS data, we can extract an estimation of the average domain size for these impurities (Figure S6, Supporting Information). Using the Debye–Scherrer equation[21] under the assumption that the domains are spherical, we obtain average domain sizes for δ-$CsPbI_3$ and δ-$FAPbI_3$ of 10–15 nm in diameter in the case of $Cs_{0.1}FA_{0.9}PbI_{2.4}Br_{0.6}$. More accurate results might be obtained by characterizing the samples with transmission electron microscopy;[22] however, this is a rather challenging task for this class of materials.

Considering that we deem $Cs_{0.1}FA_{0.9}PbI_{2.55}Br_{0.45}$ the most promising material of the family for optoelectronic applications, we wanted to verify our hypothesis that this material is structurally stable when grown as a single crystal. Single crystals were successfully grown according to a previously reported synthesis (see Figure S7, Supporting Information for a photograph of a millimeter-sized crystal).[16] The absorbance onset of this crystal (Figure 4a) starts at around 790 nm and is very similar to that of the corresponding thin film (Figure 1a). Steady-state photoluminescence is shown in Figure 4b; the emission is centered around 770 nm, which is also in accordance with the emission of the film. However, the FWHM of the emission of the crystal is slightly narrower (39 nm) than that of the thin film (51 nm), confirming the lower degree of energetic disorder.[23] In addition, the charge carrier lifetimes extracted from the long-lived component of the time-resolved photoluminescence data (Figure 4c) are longer on average, confirming the better quality of the crystal. The quality of the single crystal is also evident from the powder XRD pattern shown in Figure 4d. There are no visible impurities, and the peaks are narrower than for the thin films. The pattern features peak splitting (Figure S8, Supporting Information) and can be best fitted using a structural model with the tetragonal space group P4/*mbm*, where the refined lattice parameters are $a = b = 8.8738(4)$ Å, $c = 6.2622(4)$ Å. Space group *P*4/*mbm* is a

subgroup of the ideal cubic perovskite space group *Pm*-3*m* and corresponds to the $a^0a^0c^+$ octahedral tilting scheme in the Glazer notation.[24] The same structure has been reported for both $FAPbI_3$[25] and $FAPbBr_3$.[26] Fitting of the peak intensities is not perfect and might indicate that a degree of chemical inhomogeneity remains in the crystal.

3. Conclusion

We have studied the photophysics and phase stability of $Cs_{0.1}FA_{0.9}PbI_{2.55}Br_{0.45}$ and $Cs_{0.1}FA_{0.9}PbI_{2.4}Br_{0.6}$ in thin film form. Despite the small difference in stoichiometry, these materials differ fundamentally in terms of phase purity: $Cs_{0.1}FA_{0.9}PbI_{2.4}Br_{0.6}$ has a lower crystalline quality when deposited as thin film. By performing GIWAXS experiments, we found that the corresponding thin film has traces of the non-perovskite phases δ-$CsPbI_3$ and δ-$FAPbI_3$, which form small domains on the nanometer scale. Considering that $Cs_{0.1}FA_{0.9}PbI_{2.55}Br_{0.45}$ only has traces of δ-$FAPbI_3$, it is likely that the δ-$CsPbI_3$ impurities cause the reduced charge carrier lifetime observed in time-resolved PL measurements for the higher bromine content film. We would like to point out that established techniques such as CLSM and EDX were unable to demonstrate the existence of these impurities. We were able to synthesize $Cs_{0.1}FA_{0.9}PbI_{2.55}Br_{0.45}$ as high-quality single crystal, indicating that this material is structurally stable. The better material quality and relatively straightforward stoichiometry, combined with the similarity in bandgap to $MAPbI_3$, indicate that $Cs_{0.1}FA_{0.9}PbI_{2.55}Br_{0.45}$ has good potential for the use in optoelectronic applications.

4. Experimental Section

Thin Film Fabrication: The films were either fabricated on glass or on prepatterned indium tin oxide (ITO)-coated glass substrates, which were ultrasonically cleaned in detergent solution, deionized water, acetone, and isopropanol, sequentially. After drying them in an oven at 140 °C for about 10 min, they were treated with ultraviolet ozone (UV-O_3) plasma for 20 min. The substrates were transferred into a nitrogen-filled glovebox immediately for further processing. Solutions of 1 M $Cs_{0.1}FA_{0.9}PbI_{2.55}Br_{0.45}$ and $Cs_{0.1}FA_{0.9}PbI_{2.4}Br_{0.6}$ were made by dissolving stoichiometric amounts of PbI_2 (TCI Chemicals), $PbBr_2$ (TCI), formamidinium iodide (FAI) (TCI), and CsI (Alfa Aesar) in a mixture of N,N-dimethylformamide (DMF) (Sigma Aldrich) and dimethyl sulfoxide (DMSO) (Alfa Aesar) (4:1 v/v). Solutions were stirred overnight at room temperature before spin coating. Spin coating consisted of a first step at 1000 rpm for 10 s followed by a second step of 4000 rpm for 30 s. Chlorobenzene (Sigma Aldrich) was dropped as antisolvent 5 s prior to the end of the second step. Afterward, the samples were annealed at 100 °C for 10 min. The resulting films had a thickness of around 450–500 nm.

Crystal Synthesis: To synthesize $FA_{0.9}Cs_{0.1}PbI_{2.55}Br_{0.45}$, a 0.8 M solution with respect to [Pb] was prepared. Thus, in 11.25 mL of gamma-butyrolactone (Acros, 99+%), 1.39 g of formamidinium iodide (FAI) (prepared as described in earlier work),[16] 0.23 g of CsI (ABCR, 99.9%), 3.22 g of PbI_2 (Sigma Aldrich, 99%), and 0.74 g of $PbBr_2$ (Acros, 98+%) were dissolved, generating a yellow solution. The solution was filtered through a 0.2 μm syringe filter and distributed over three 20 mL vials with a cap. The vessels were next placed in a glycerol bath preheated to 90 °C and then heated to 115 °C at a rate of 5 °C h^{-1}, keeping them at 115 °C for an additional 1 h. Next, the crystals were separated from the hot solution, dried with a filter paper, and placed in a desiccator over $CaCl_2$.

Characterization: Thin film absorption measurements were conducted with a Shimadzu UV-3600 spectrophotometer with an integrating sphere attachment. UV–vis absorbance spectra of the microcrystalline powders were collected using a Jasco V670 spectrophotometer equipped with a halogen lamp and an integrating sphere (ILN-725) with a working wavelength range of 220–2200 nm. Barium sulfate ($BaSO_4$) was used as a reference for diffuse reflectance. The absorbance spectrum of the single crystal was estimated from reflectance and transmittance spectra collected from a thin layer of crystal that was ground into powder deposited between the glass slides. For the photoluminescence measurements, the second harmonic (400 nm) of a mode-locked Ti:sapphire laser was used as an excitation source. A pulse picker was inserted in the optical path to decrease the repetition rate of the laser pulses when needed. The laser power at the sample was adjusted by neutral density filters. The excitation beam was focused with a 150-mm focal length lens, and the fluorescence was collected by the same lens and then coupled into a spectrometer. The spectra were recorded using an Image EM CCD camera (Hamamatsu, Japan). Time-resolved PL spectra were measured using a Hamamatsu streak camera working in single sweep mode. CLSM was performed using an inverted Nikon Ti-eclipse microscope equipped with a Nikon C1 scan head. A CW laser with a wavelength of 488 nm was used as an excitation source and was focused onto the sample using a 40× ELWD objective. The photoluminescence from the sample was collected by raster scanning the excitation beam over the surface and recording the PL at each point using photomultiplier tubes operating in three different wavelength regimes: 515 ± 30, 590 ± 50, and 780 nm long-pass. Atomic force microscopy images were acquired with a Bruker Dimension Icon using ScanAsyst mode. The XRD was performed under ambient conditions using a Bruker D8 Advance diffractometer in Bragg–Brentano geometry, and operating with a Cu Kα radiation source ($\lambda = 1.54$ Å) and a Lynxeye detector. The powder XRD pattern of the crystal was collected in transmission mode (Debye–Scherrer geometry) with a STADI P diffractometer (STOE&Cie GmbH), equipped with a curved Ge (111) monochromator (Cu Kα1 = 1.54 Å) and a silicon strip MYTHEN 1K detector (Fa. DECTRIS). For the measurement, the ground crystals were placed between Mylar foils with a small drop of paraffin oil. EDX maps and spectra were obtained using an FEI Nova Nano SEM 650 with an accelerating voltage of 15 kV. The Goldschmidt tolerance factor of the perovskite was calculated according to the ionic radii and formulas as described by Sun et al.[27] GIWAXS measurements were performed using a MINA X-ray scattering instrument built on a Cu rotating-anode source ($\lambda = 1.5413$ Å). The 2D patterns were collected using a Vantec500 detector (1024 × 1024 pixel array with pixel size of 136 × 136 μm) located 93 mm away from the sample. The perovskite films were placed in reflection geometry at certain incident angles α_i with respect to the direct beam using a Huber goniometer. GIWAXS patterns were acquired using a variable incident angle in the range of 0.4–2.2° to probe the thin film structure at an X-ray penetration depth ranging from close to the surface to the entire film thickness. For an ideally flat surface, the value of the X-ray penetration depth (i.e., the depth into the material measured along the surface normal where the intensity of X-rays falls to $1/e$ of its value at the surface) depends on the X-ray energy (wavelength λ), the critical angle of total reflection, α_c, and the incident angle, α_i, and can be estimated using the relation: $\Lambda = \frac{\lambda}{4\pi}\sqrt{\frac{2}{(\alpha_i^2-\alpha_c^2)^2+4\beta^2-(\alpha_i^2-\alpha_c^2)}}$, where β is the imaginary part of the complex refractive index of the compound. The direct beam center position on the detector and the sample-to-detector distance were calibrated using the diffraction rings from standard silver behenate and Al_2O_3 powders. All the necessary corrections for the GIWAXS geometry were applied to the raw patterns using the FIT2D and the GIXGUI MATLAB toolbox. The GIWAXS patterns are presented as a function of the horizontal q_y and quasivertical q_z scattering vector

$$q_y = \frac{2\pi}{\lambda}(\sin(2\theta_f)\cos(\alpha_f)); q_z = \frac{2\pi}{\lambda}(\sin(\alpha_i) + \sin(\alpha_f)) \quad (1)$$

where $2\theta_f$ is the scattering angle in the horizontal direction and α_f is the exit angle in the vertical direction. Radial integration of the GIWAXS

patterns leads to the integrated intensity $I(q)$ versus q, where q is the modulus of the scattering vector: $q = \frac{4\pi}{\lambda}\sin(\theta)$.

Supporting Information

Supporting Information is available from the Wiley Online Library or from the author.

Acknowledgements

The authors thank A. Kamp and T. Zaharia for technical support. This work is part of the research program of the Netherlands Organisation for Scientific Research (NWO). This is a publication of the FOM-focus group "Next Generation Organic Photovoltaics," participating in the Dutch Institute for Fundamental Energy Research (DIFFER).

Conflict of Interest

The authors declare no conflict of interest.

Keywords

perovskites, photophysics, single crystals, stoichiometry, thin films

Received: August 30, 2019
Revised: October 15, 2019
Published online:

[1] Best Research-Cell Efficiency Chart | Photovoltaic Research | NREL, https://www.nrel.gov/pv/cell-efficiency.html (accessed: October 2019).
[2] L. Chen, Y.-Y. Tan, Z.-X. Chen, T. Wang, S. Hu, Z.-A. Nan, L.-Q. Xie, Y. Hui, J.-X. Huang, C. Zhan, S.-H. Wang, J.-Z. Zhou, J.-W. Yan, B.-W. Mao, Z.-Q. Tian, *J. Am. Chem. Soc.* **2019**, *141*, 1665.
[3] J.-W. Lee, D.-H. Kim, H.-S. Kim, S.-W. Seo, S. M. Cho, N.-G. Park, *Adv. Energy Mater.* **2015**, *5*, 1501310.
[4] Q. Ma, S. Huang, S. Chen, M. Zhang, C. F. J. Lau, M. N. Lockrey, H. K. Mulmudi, Y. Shan, J. Yao, J. Zheng, X. Deng, K. Catchpole, M. A. Green, A. W. Y. Ho-Baillie, *J. Phys. Chem. C* **2017**, *121*, 19642.
[5] M. Saliba, T. Matsui, J.-Y. Seo, K. Domanski, J.-P. Correa-Baena, M. K. Nazeeruddin, S. M. Zakeeruddin, W. Tress, A. Abate, A. Hagfeldt, M. Grätzel, *Energy Environ. Sci.* **2016**, *9*, 1989.
[6] F. Ruf, P. Rietz, M. F. Aygüler, I. Kelz, P. Docampo, H. Kalt, M. Hetterich, *ACS Energy Lett.* **2018**, *3*, 2995.
[7] D. P. McMeekin, G. Sadoughi, W. Rehman, G. E. Eperon, M. Saliba, M. T. Horantner, A. Haghighirad, N. Sakai, L. Korte, B. Rech, M. B. Johnston, L. M. Herz, H. J. Snaith, *Science* **2016**, *351*, 151.
[8] C. M. Sutter-Fella, Q. P. Ngo, N. Cefarin, K. L. Gardner, N. Tamura, C. V. Stan, W. S. Drisdell, A. Javey, F. M. Toma, I. D. Sharp, *Nano Lett.* **2018**, *18*, 3473.
[9] Z. Li, M. Yang, J.-S. Park, S.-H. Wei, J. J. Berry, K. Zhu, *Chem. Mater.* **2016**, *28*, 284.
[10] S. Shao, M. Abdu-Aguye, T. S. Sherkar, H.-H. Fang, S. Adjokatse, G. ten Brink, B. J. Kooi, L. J. A. Koster, M. A. Loi, *Adv. Funct. Mater.* **2016**, *26*, 8094.
[11] T. Salim, S. Sun, Y. Abe, A. Krishna, A. C. Grimsdale, Y. M. Lam, *J. Mater. Chem. A* **2015**, *3*, 8943.
[12] Z. Lian, Q. Yan, Q. Lv, Y. Wang, L. Liu, L. Zhang, S. Pan, Q. Li, L. Wang, J.-L. Sun, *Sci. Rep.* **2015**, *5*, 16563.
[13] H.-H. Fang, S. Adjokatse, H. Wei, J. Yang, G. R. Blake, J. Huang, J. Even, M. A. Loi, *Sci. Adv.* **2016**, *2*, e1600534.
[14] V. M. Goldschmidt, *Naturwissenschaften* **1926**, *14*, 477.
[15] K. A. Bush, A. F. Palmstrom, Z. J. Yu, M. Boccard, R. Cheacharoen, J. P. Mailoa, D. P. McMeekin, R. L. Z. Hoye, C. D. Bailie, T. Leijtens, I. M. Peters, M. C. Minichetti, N. Rolston, R. Prasanna, S. Sofia, D. Harwood, W. Ma, F. Moghadam, H. J. Snaith, T. Buonassisi, Z. C. Holman, S. F. Bent, M. D. McGehee, *Nat. Energy* **2017**, *2*, 17009.
[16] O. Nazarenko, S. Yakunin, V. Morad, I. Cherniukh, M. V. Kovalenko, *NPG Asia Mater.* **2017**, *9*, e373.
[17] J.-F. Liao, H.-S. Rao, B.-X. Chen, D.-B. Kuang, C.-Y. Su, *J. Mater. Chem. A* **2017**, *5*, 2066.
[18] J. S. Han, Q. Van Le, J. Choi, K. Hong, C. W. Moon, T. L. Kim, H. Kim, S. Y. Kim, H. W. Jang, *Adv. Funct. Mater.* **2018**, *28*, 1705783.
[19] W. Mao, C. R. Hall, A. S. R. Chesman, C. Forsyth, Y.-B. Cheng, N. W. Duffy, T. A. Smith, U. Bach, *Angew. Chem. Int. Ed.* **2019**, *58*, 2893.
[20] T. J. Jacobsson, S. Svanström, V. Andrei, J. P. H. Rivett, N. Kornienko, B. Philippe, U. B. Cappel, H. Rensmo, F. Deschler, G. Boschloo, *J. Phys. Chem. C* **2018**, *122*, 13548.
[21] D.-M. Smilgies, *J. Appl. Crystallogr.* **2009**, *42*, 1030.
[22] Y. Zhou, H. Sternlicht, N. P. Padture, *Joule* **2019**, *3*, 641.
[23] M. Vrućinić, C. Matthiesen, A. Sadhanala, G. Divitini, S. Cacovich, S. E. Dutton, C. Ducati, M. Atatüre, H. Snaith, R. H. Friend, H. Sirringhaus, F. Deschler, *Adv. Sci.* **2015**, *2*, 1500136.
[24] A. M. Glazer, *Acta Crystallogr. Sect. B Struct. Crystallogr. Cryst. Chem.* **1972**, *28*, 3384.
[25] D. H. Fabini, C. C. Stoumpos, G. Laurita, A. Kaltzoglou, A. G. Kontos, P. Falaras, M. G. Kanatzidis, R. Seshadri, *Angew. Chem. Int. Ed.* **2016**, *55*, 15392.
[26] E. C. Schueller, G. Laurita, D. H. Fabini, C. C. Stoumpos, M. G. Kanatzidis, R. Seshadri, *Inorg. Chem.* **2018**, *57*, 695.
[27] Y. Sun, J. Peng, Y. Chen, Y. Yao, Z. Liang, *Sci. Rep.* **2017**, *7*, 46193.